Progress In Electromagnetics Research, Vol. 140, 653–680, 2013

CIRCULARLY ARCED KOCH FRACTAL MULTIBAND MULTIMODE MONOPOLE ANTENNA

Daotie Li* **and Junfa Mao**

Key Laboratory of Ministry of Education of China for Research and Design of Electromagnetic Compatibility of High Speed Electronic Systems, Shanghai Jiao Tong University, Shanghai 200240, China

Abstract—Circularly arced Koch fractal curve (CAKC) is originally proposed. Then, a novel wire dipole is formed with K_i-iterated CAKC. The dipole is experimentally studied for fractal electrical characteristics revealing. It manifests many unique properties, such as multiband resonance at odd times of half-wavelength. In particular, it unprecedentedly presents normal mode ($0.5 \cdot \lambda$) and axial mode ($1.5 \cdot \lambda$) simultaneously. Thus, $\mathbf{K}_2$ CAKC wire is configured into folded monopole with circular disc ground for omni-directional and directive radiation. Five matched bands ($|S_{11}| \leq -10\,\text{dB}$) are obtained within 1 GHz–10 GHz, of which $f_1 = 1.31\,\text{GHz}$, $f_2 = 3.14\,\text{GHz}$, $f_3 = 3.63\,\text{GHz}$, $f_4 = 4.65\,\text{GHz}$, and $f_5 = 7.71\,\text{GHz}$. Compared with straight wire monopole ($0.25 \cdot \lambda$), this fractal monopole shows 31% height reduction. It has dipole-like patterns at f_1 and f_2, endfire patterns at f_3 and f_4 with high gain (10 dBi), and off-endfire patterns at f_5. Moreover, the fractal antenna possesses compactness, lightweight, simplicity, and low cost. So, it is an attractive candidate for multiband and multifunction antennas, such as satellite antennas, of which omni-directional normal mode and directive axial mode are needed for beaconing and communication respectively.

1. INTRODUCTION

The fractal antenna has drawn much attention since it was put forth in 1995 by Nathan Cohen [1, 2]. It is a combination of antenna technology and fractal geometry [3–5] and has shown many particular attributes as concluded in [6, 7]. However, the fractal antenna has

Received 4 April 2013, Accepted 31 May 2013, Scheduled 27 June 2013

* Corresponding author: Daotie Li (3460023@qq.com).

not gained further theoretical breakthrough in recent years. The major challenges for fractal antennas are arbitrary frequency ratio [8–10], wideband or ultra-wideband, radiation pattern improvement, and consistency of impedance, directivity and polarization in multiband or ultra-broadband.

Mathematically, fractal or fractus is a highly complex, irregular or broken geometry [11, 12]. Just as its name implies, it consists of similar-shaped or affine pieces of different scales, which usually cannot be represented with a continuous function. With these exquisite structures, fractal is able to yield more ideal diversiform current distribution, so a fractal-shaped antenna generally has better radiation properties than Euclidean counterparts. Thus far, almost all fractal antennas comprise fractal geometries with straight segments or rectilinearly-edged blocks, such as Koch curve series [13–15], Minkowski curve [16], and Sierpinski Carpet series [8, 17–20]. Naturally, we conceive the idea of fabricating a fractal antenna with curved elements, such as circular or elliptical arc with hope of further enhancing performances — bandwidth, directivity, and gain. In this paper, we propose a novel circularly arced Koch fractal curve (CAKC). Then, we model and simulated CAKC wire dipoles of each iteration with IE-MOM (Integration Equations solved by Method of Moment) solver of commercial electromagnetic software Ansoft HFSS$^{\text{TM}}$ v.13. Compared with conventional Koch counterparts, CAKC dipole has more size reduction, smaller frequency ratio. In particular, it has normal mode ($0.5 \cdot \lambda$) and axial mode ($1.5 \cdot \lambda$) simultaneously. The discovery of $1.5 \cdot \lambda$ axial mode will further extend applications of dipole and monopole antennas.

Thus, a $\mathbf{K}_2$-iterated CAKC folded monopole with a circular disc ground and directly fed by a $50\,\Omega$ coaxial cable is designed, fabricated, and measured. Good agreement is obtained from simulation and measurement. This monopole uniquely has penta-bands and tri-modes, of which $f_1 = 1.31\,\text{GHz}$ and $f_2 = 3.14\,\text{GHz}$ both have dipole-like patterns (axial null, normal mode), $f_3 = 3.63\,\text{GHz}$ and $f_4 = 4.65\,\text{GHz}$ both have endfire patterns (axial peak, axial mode), and $f_5 = 7.71\,\text{GHz}$ has off-endfire pattern (off-axial peak without null). In contrast, Euclidean wire and other fractal wire monopoles have only dipole-like patterns. In addition, the proposed fractal monopole has 31% height shrinkage at fundamental resonance f_1 and 25.94% broad bandwidth at the highest resonance f_5. The peculiar multiband and multimode properties make it a very comparative candidate for applications like omni-directional and directive communications, such as satellite beaconing and point-to-point communications.

The peculiarities of circularly-curved fractus manifest its great

advantages and potentiality in performance enhancement of fractal antennas.

2. CIRCULARLY ARCED KOCH CURVES (CAKC)

CAKC is similar to Koch curve in the panorama and iterative process, only the initiator and the generator are replaced with circular arcs. Therefore, the iterative procedure will be introduced briefly. It begins with a semicircular arc initiator $\mathbf{K}_0$ of radius d_0, as shown in Fig. 1(a), then $\mathbf{K}_0$ transits into $\mathbf{K}_1$ by replacing the semi-arc with three semicircular arcs of radius $d_1 = d_0/3$, as shown in Fig. 1(b). From $\mathbf{K}_2$

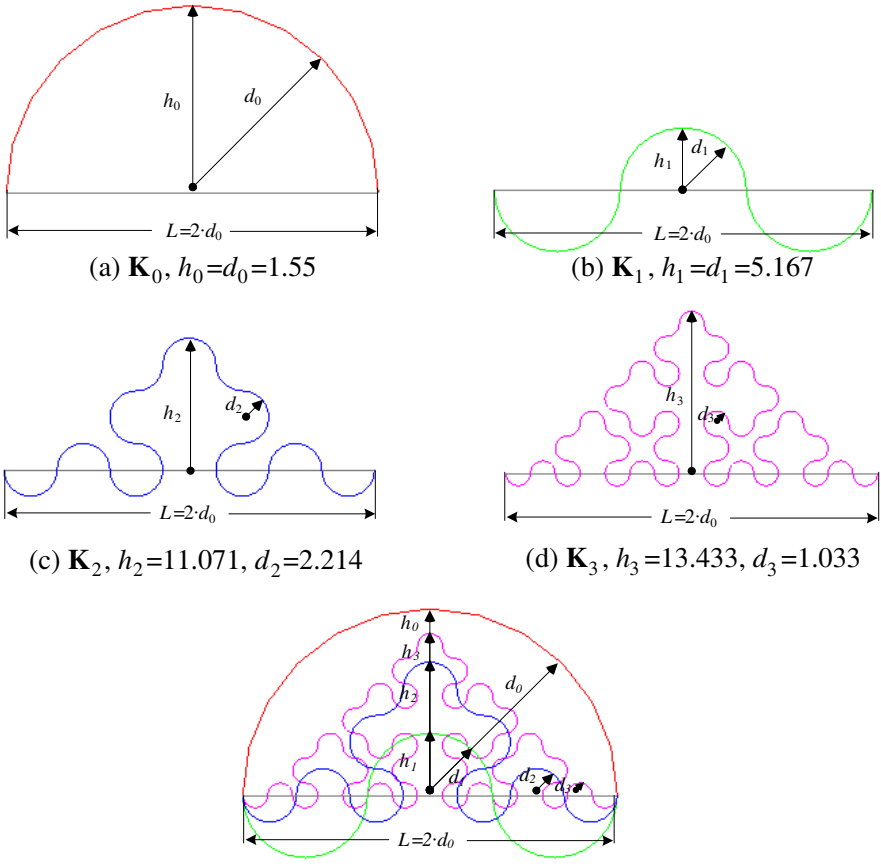

(a) $\mathbf{K}_0$, h_0=d_0=1.55

(b) $\mathbf{K}_1$, h_1=d_1=5.167

(c) $\mathbf{K}_2$, h_2=11.071, d_2=2.214

(d) $\mathbf{K}_3$, h_3=13.433, d_3=1.033

(e) Superposition of all iterations

Figure 1. K_i CAKC (unit: mm).

on, the procedure has a little difference from that of Koch curve. The lateral arcs repeat the process while the middle one is superseded by a smoothly arched segment, which comprises 5 semicircular arcs, as shown in Figs. 1(c)–(d). This procedure proceeds to form CAKC of each iteration, as shown in Figs. 1(a)–(e). CAKC is fully parameterized and modeled with Ansoft HFSS$^{\mathrm{TM}}$ v.13. All the shape parameters have close relativity during iteration, as depicted in formula (1)–(7).

Numbers of arc segments of successive iterations have the following relationships:

$$N_{i+1} = 4 \cdot N_i - 1 \quad (i = 0, 1, 2, \ldots, n;\ N_0 = 1) \tag{1}$$

$$M_{i+1} = 2 \cdot M_i + 1 \quad (i = 0, 1, 2, \ldots, n;\ M_0 = 1) \tag{2}$$

where N_i denotes the total number of arcs of the ith-iterated CAKC and M_i the equivalent number of arcs in the length direction (X-axis). Circular arc radius d_i and overall height of each iteration above the horizontal baseline (grey straight line in Figs. 1(a)–(d).) h_i is:

$$d_i = \frac{d_0}{2^{i+1} - 1} \quad (i = 0, 1, 2, \ldots, n) \tag{3}$$

and

$$h_i = (2 \cdot k_{i-1} + 3) \cdot d_i = \left(\frac{2^{i-1} + 3 \cdot \sum_{k=2}^{i} 2^{i-k}}{2^{i+1} - 1} \right) \cdot d_0 \ \ (i = 0, 1, 2, \ldots, n)$$

$$\lim_{i \to \infty} h_i = +\infty \quad (i = 2, 3, \ldots, n;\ k_0 = k_1 = 1) \tag{4}$$

respectively. Obviously, h_i increases infinitely with iterative process. According to definition of box dimension [9, 10], we obtain the fractal dimension as follows:

$$D_F = -\lim_{i \to \infty, \delta \to 0} \frac{\log Ni + 1}{\log \delta_{i+1}} = -\lim_{i \to \infty, \delta \to 0} \frac{\log 2 \cdot (4 \cdot Ni - 1)}{\log \frac{\pi}{2} \cdot \left(\frac{d_0}{2^{i+1} - 1} \right)} = 2$$

$$(N_0 = 1,\ i = 0, 1 \ldots, n) \tag{5}$$

Then, we obtain physical scale ratio ζ_i:

$$\lim_{i \to \infty} \zeta_i = \lim_{i \to \infty} \frac{N_i \cdot \left(\pi \cdot \frac{d_0}{2^{i+1} - 1} \right)}{N_{i-1} \cdot \left(\pi \cdot \frac{d_0}{2^{(i-1)+1} - 1} \right)} = \frac{(4 \cdot N_{i-1} - 1)}{N_{i-1}} \cdot \frac{\left(2^i - 1\right)}{2^{i+1} - 1} = 2 \tag{6}$$

and fractal scale ratio σ_i:

$$\lim_{i \to \infty} \sigma_i = \frac{M_i \cdot \left(\pi \cdot \frac{d_0}{2^{i+1} - 1} \right)}{M_{i-1} \cdot \left(\pi \cdot \frac{d_0}{2^{i+1} - 1} \right)} = \frac{2 \cdot M_{i-1} + 1}{M_{i-1}} \approx 2 \tag{7}$$

As shown in formulas (5)–(7), fractal dimension D_F, physical scale ratio ζ_i, and fractal scale ratio σ_i are coincidentally identical. This circumstance is very infrequent with all well-known fractals. And this property might intimately associate with the antenna's performance. Radius of dipole wire of each iteration r_i is:

$$r_i = \frac{r_0}{2^{i-1}} \quad (i = 1, 2, 3, \ldots, n;\ r_0 = 2) \tag{8}$$

From formula (8), we can see the radius of wire decreases with iterative number K_i. This is the main reason that the maximum iterative times of a fractal wire antenna is usually chosen as a small natural number, as 2 to 5 times at most, or else the fractal wire or stripe will be self-overlapped or infinitesimal [21], as illustrated in Fig. 2. The relationship between radius and iteration could have other forms except the form in equation (8). But no matter what form it has, radius diminishes with iteration consequentially.

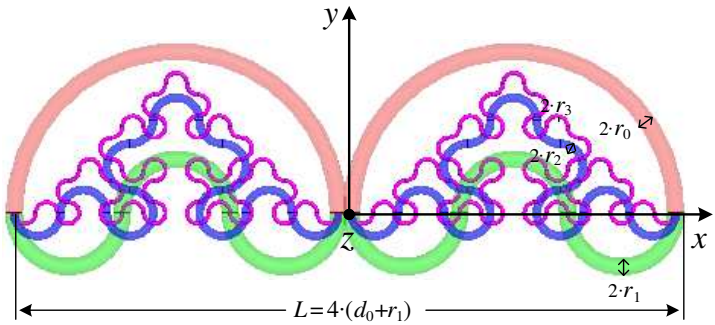

Figure 2. K_i CAKC wire dipoles (red-$\mathbf{K}_0$, green-$\mathbf{K}_1$, blue-$\mathbf{K}_2$, magenta-$\mathbf{K}_3$).

Geometry of CAKC can be absolutely determined by Equations (1)–(8). Electrical properties of a wire antenna based on the fractal curve are also associated with these shape parameters. For instance, physical scale ratio ζ_i determines total length of the curve. Consequently, the fundamental resonance frequency f_1, which depends upon the overall dimension, can be decided with appropriate selection of ζ_i, initial length L, and iteration K_i. The fractal dimension D_F is relevant to resonance frequency, bandwidth, and input impedance somehow, which can be validated with formula (9). An antenna designer can approximately evaluate the fundamental resonance f_1, which is dipole-like pattern (normal mode, $0.5 \cdot \lambda_1$), and the second resonance f_2, which is end-fire pattern (axial mode, $1.5 \cdot \lambda_2$), of a CAKC wire dipole according to the conclusions above.

3. CAKC DIPOLE ANTENNAS

3.1. Brief Review of Dipole Antennas

Dipole and monopole have been widely applied due to their simplicity, ease, and low-cost for design and fabrication. All well-known fractal curves, such as Koch curve [13], Peano curve [22], Giuseppe Peano curve [17], and Hilbert Curve [23, 24], are preferably designed into dipole or monopole antennas. So, CAKC wire is also fed at the endpoint to form a dipole or monopole antenna, as shown in Fig. 2.

Up to now, almost all wire antennas are evolved from the original Hertz half-wavelength dipole. A centre-fed thin straight wire dipole antenna has many electrical sizes, but only the half-wavelength is available. It has sinusoidal-like current distribution J_s on the dual arms, as depicted in Figs. 3(a)–(d). J_s maximizes on the feeding point only when electrical size is approximate to odd-times half-wavelength (resonance), such as $0.5 \cdot \lambda$, $1.5 \cdot \lambda$. It suggests that the dipole has lower and matchable input impedance in these wavelengths ($0.5 \cdot \lambda - Z_{in} = 73\,\Omega$, $1.5 \cdot \lambda - Z_{in} = 118\,\Omega$), as shown in Fig. 4. Gain pattern is another important concern. The dipole has normal omni-directivity radiation mode (round-shaped in H-plane, doughnut-shaped in E-plane) when $L \leq 1 \cdot \lambda$. The E-pattern becomes cloven when electrical size grows, such as quarter-foiled in $1.25 \cdot \lambda$, hexa-foiled in $1.5 \cdot \lambda$, as depicted in Figs. 5 (a)–(b). Like half-wavelength, the full-wavelength also has an omnidirectional pattern, but the gain is 1.67 dBi higher (3.82 dBi–2.15 dBi). However, it has very high impedance ($> 2.5\,\mathrm{k}\Omega$) because feeding point is just the null of J_s, which means great difficulty in matching with $50\,\Omega$.

In conclusion, half-wavelength is the only usable electrical size of a wire dipole, no matter Euclidean-shaped or rectilinear fractal-shaped. So, the novel CAKC is proposed to transform wire dipole with the

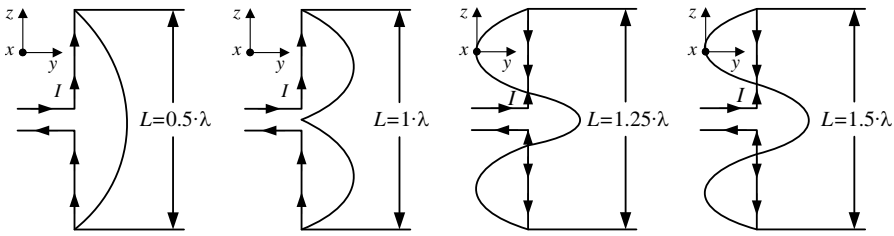

Figure 3. Current distribution on a straight wire dipole.

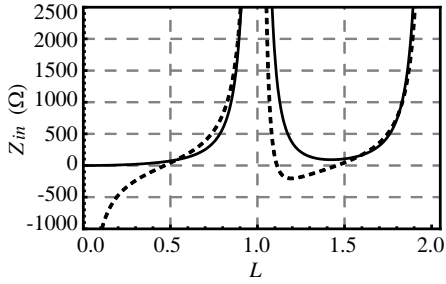

Figure 4. Input impedance Z_{in} of a straight wire dipole (solid-R_{in}, dash-X_{in}; $0.5\cdot\lambda - Z_{in} = 73\,\Omega$, $1\cdot\lambda - Z_{in} > 2.5\,\mathrm{k}\Omega$, $1.5\cdot\lambda - Z_{in} = 118\,\Omega$).

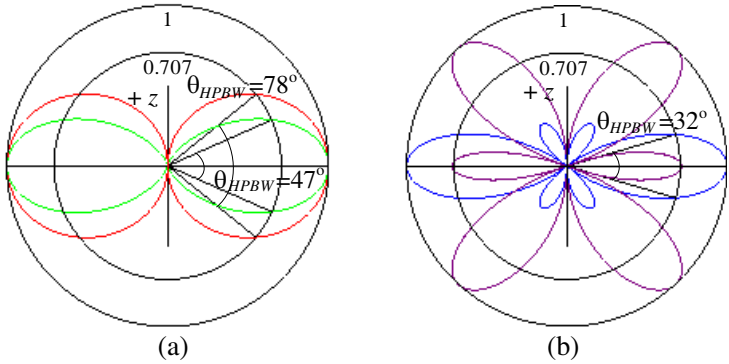

Figure 5. E-plane pattern of a conventional wire dipole (G = 2.15 dBi, 3.82 dBi, 5.16 dBi, 3.48 dBi in $L = 0.5\cdot\lambda$, $1\cdot\lambda$, $1.25\cdot\lambda$, $1.5\cdot\lambda$, respectively; dipole oriented in Z-axis). (a) Red-$L = 0.5\cdot\lambda$, green-$L = 1\cdot\lambda$. (b) Blue-$L = 1.25\cdot\lambda$, purple-$L = 1.5\cdot\lambda$.

hope of more electrical sizes, such as $1.5\cdot\lambda$, $2.5\cdot\lambda$, can be available simultaneously.

3.2. Simulation Results of CAKC Dipole Antennas

$\mathbf{K}_0$–$\mathbf{K}_3$ CAKCs with length $L = 4\cdot(d_0 + r_i)$, arc radius d_i, and wire diameter $2\cdot r_i$ ($d_0 = 15.5\,\mathrm{mm}$, $r_0 = 0.5\,\mathrm{mm}$) are configured into dipoles in specular symmetry, as depicted in Fig. 2. Then, the dipoles are experimentally investigated with IE-MOM solver (Integration Equations solved by Method of Moment) of Ansoft HFSS$^{\mathrm{TM}}$ v.13 in band 1 GHz–10 GHz, as illustrated in Figs. 6–7. They are fed on the ends of the fractal wires with a fixed gap $H_g = 0.1\,\mathrm{mm}$ in free space.

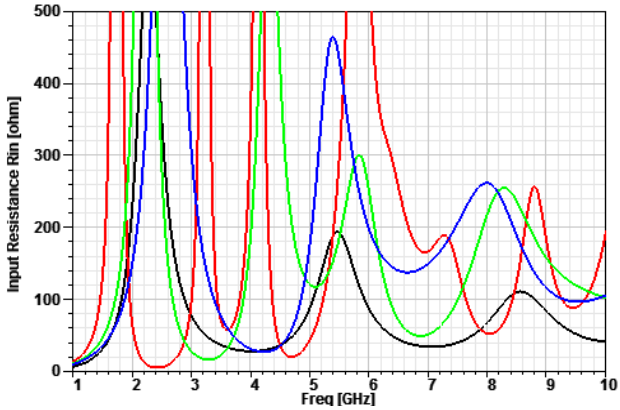

Figure 6. Input resistance $R_{in}(f)$ of K_i CAKC ($\mathbf{K}_0$-black, $\mathbf{K}_1$-blue, $\mathbf{K}_2$-green, $\mathbf{K}_3$-red).

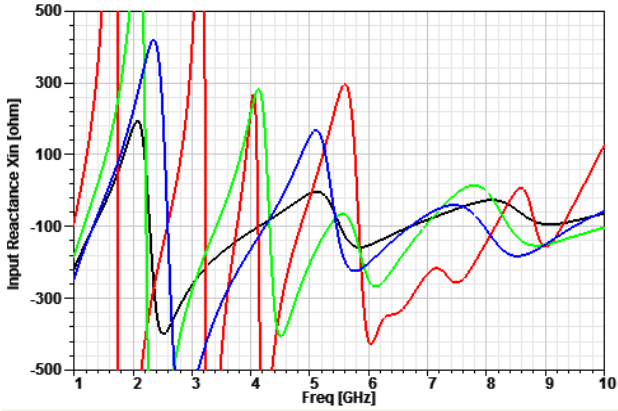

Figure 7. Input reactance $X_{in}(f)$ of K_i CAKC ($\mathbf{K}_0$-black, $\mathbf{K}_1$-blue, $\mathbf{K}_2$-green, $\mathbf{K}_3$-red).

For ideal impedance match, resonant impedances of f_{ij} (i-K_i, j-jth resonant frequency of K_i) are chosen as the port impedances, so that fractal properties of the fractal dipoles will be better revealed. During iteration, they present distinct fractal electrical properties in input impedance Z_{in}, bandwidth BW and radiation pattern G, as shown in Figs. 6–11. All the resonant properties are tabulated in Table 1.

Table 1. Simulated resonant properties of K_i CAKC dipoles.

$\mathbf{K}_0$	f_i **(GHz)**	f_1	f_2	f_3	
		1.6319	5.1256	8.0724	
	$\delta_n = f_{n+1}/f_n$	—	3.1409	1.5749	
	R_{in} **(Ω)**	47.34	117.13	75.45	
	BW (MHz)	151.7, 9.30%	584.5, 11.40%	700, 8.67%	
	Gain (dBi)	2.057	2.4801	3.1921	
$\mathbf{K}_1$	f_i **(GHz)**	f_1	f_2		
		1.5782	4.5866		
	$\delta_n = f_{n+1}/f_n$	—	2.9066		
	R_{in} **(Ω)**	43.27	42.92		
	BW (MHz)	132, 8.37%	170, 3.71%		
	Gain (dBi)	2.0106	0.5937		
$\mathbf{K}_2$	f_i **(GHz)**	f_1	f_2	f_3	
		1.3774	3.6525	7.5495	
	$\delta_n = f_{n+1}/f_n$	—	2.6517	2.0669	
	R_{in} **(Ω)**	31.8513	37.1771	109.621	
	BW (MHz)	82, 6.13%	102, 2.79%	700, 9.27%	
	Gain (dBi)	1.916	1.4353	-1.9406	
$\mathbf{K}_3$	f_i **(GHz)**	f_1	f_2	f_3	f_4
		1.1218	2.7212	5.0425	9.5940
	$\delta_n = f_{n+1}/f_n$	—	2.4257	1.8530	1.9026
	R_{in} **(Ω)**	20.5256	16.4617	50.5181	95.4681
	BW (MHz)	34, 3.03%	28, 1.03%	125, 2.48%	393, 4.1%
	Gain (dBi)	1.8643	3.8811	1.7044	3.159

3.3. Discussion on CAKC Dipoles

Figure 8 shows that f_1 of K_i CAKC ($i = 0, 1, 2, 3, \ldots$) displays dipole-like gain patterns ($0.5 \cdot \lambda$), which are doughnut-shaped in XOZ (E-plane, Phi = 0°) and omnidirectional in YOZ (H-plane, Phi = 90°). This indicates that f_1 is the fundamental resonant frequency of the multiband dipoles. Gain patterns of K_i at f_2 present remarkable

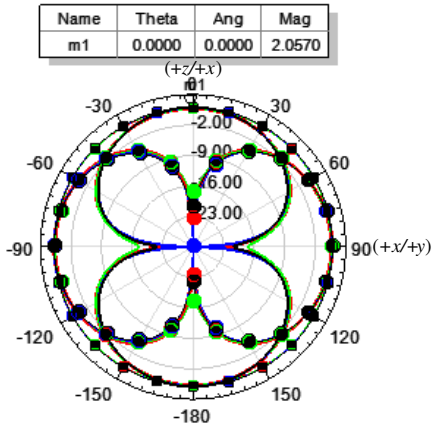

Figure 8. Gain patterns of K_i at f_1 (bare solid-Phi = 0°, XOZ, E-plane; box marked solid-Phi = 90°, YOZ, H-plane; circle marked solid-Theta = 90°, XOY; $\mathbf{K}_0$-black, $\mathbf{K}_1$-blue, $\mathbf{K}_2$-green, $\mathbf{K}_3$-red, as shown in Table 1).

difference. $\mathbf{K}_0$ and $\mathbf{K}_1$ show similar dipole-like gain patterns, while $\mathbf{K}_2$ and $\mathbf{K}_3$ peculiarly shows a similar peanut-shaped gain pattern with maximum radiation in the axial direction (X-axis, $1.5 \cdot \lambda$), in which the pattern nulls emerge for almost all conceived dipoles or monopoles of half-wavelength up to the present, as shown in Figs. 9(a)–(c). The directivity is enhanced gradually in this direction with iteration. This radiation property is unprecedented and means that K_i CAKC fractal can be designed as a normal mode and axial mode multiband monopole simultaneously by being backed with a ground plate. Gain patterns of K_i at f_3 also present conspicuous discrepancy. $\mathbf{K}_0$ and $\mathbf{K}_2$ show similar quatrefoil-shaped gain patterns with maximum radiation in lateral direction ($+Y$-axis), while $\mathbf{K}_3$ shows elliptoid gain pattern with maximum radiation in the axial direction (X-axis), as shown in Figs. 10(a)–(c). Gain pattern of $\mathbf{K}_3$ at f_4 also displays axial maximum (X-axis). But it is cross-shaped in XOZ (E-plane, Phi = 0°) and quasi-omnidirectional in YOZ (H-plane, Phi = 90°), as shown in Fig. 11. In addition, compared with its Euclidean and rectilinear fractal comparators, CAKC dipole has no side lobes in the radiation patterns.

Then, we illustrate surface current density distribution J_s of resonant frequencies of $\mathbf{K}_3$ dipole in Figs. 12–15. With the distribution, we can intuitively unveil the fractal trait in essence. For a better view, only left arm of the dipole is displayed.

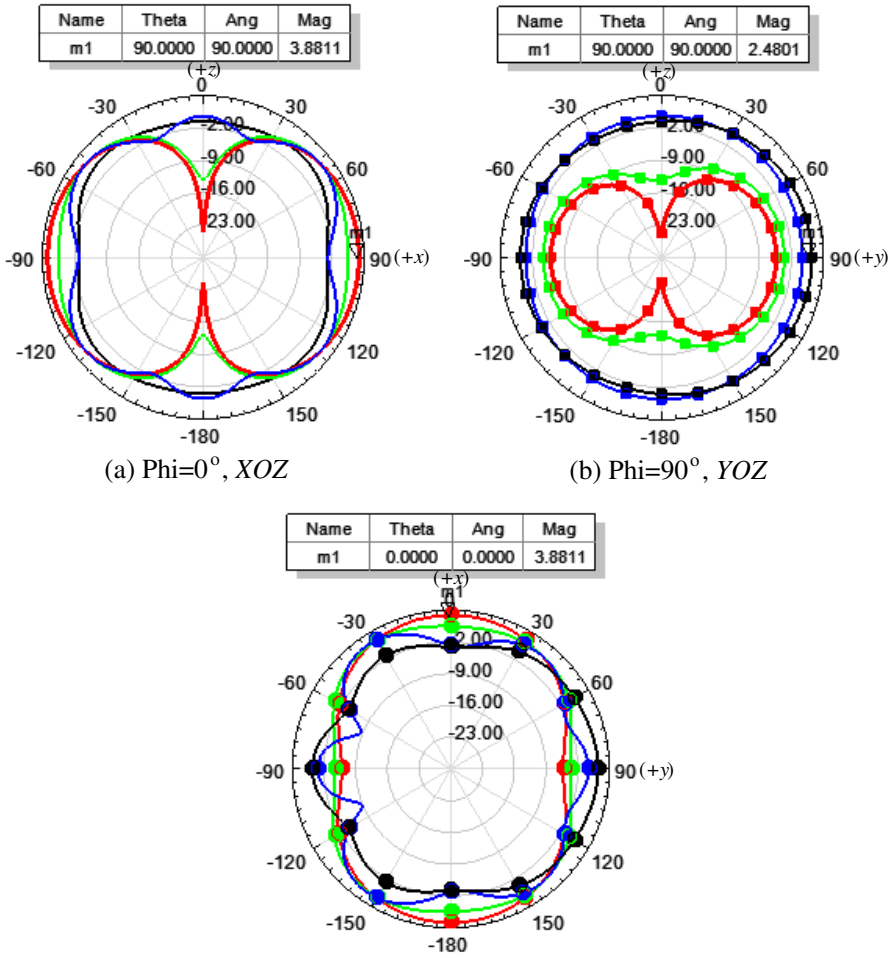

(a) Phi=0°, *XOZ* (b) Phi=90°, *YOZ*

(c) Theta=90°, *XOY*

Figure 9. Gain patterns of K_i at f_2 (bare solid-Phi = 0°, XOZ, E-plane; box marked solid-Phi = 90°, YOZ; circle marked solid-Theta = 90°, XOY, H-plane; $\mathbf{K}_0$-black, $\mathbf{K}_1$-blue, $\mathbf{K}_2$-green, $\mathbf{K}_3$-red, as shown in Table 1).

From J_s depicted in Figs. 12–15, we can see that $\mathbf{K}_3$ CAKC dipole operates in odd-numbered half-wavelength, namely f_1 is $1 \cdot \lambda/2$, f_2 $3 \cdot \lambda/2$, f_3 $7 \cdot \lambda/2$, and f_4 $15 \cdot \lambda/2$, of which f_1 is normal mode, f_2 and f_3 the axial modes, and f_4 the mixed mode of normal and axial. Comparably, all conventional dipoles, no matter wire or sheet, narrow

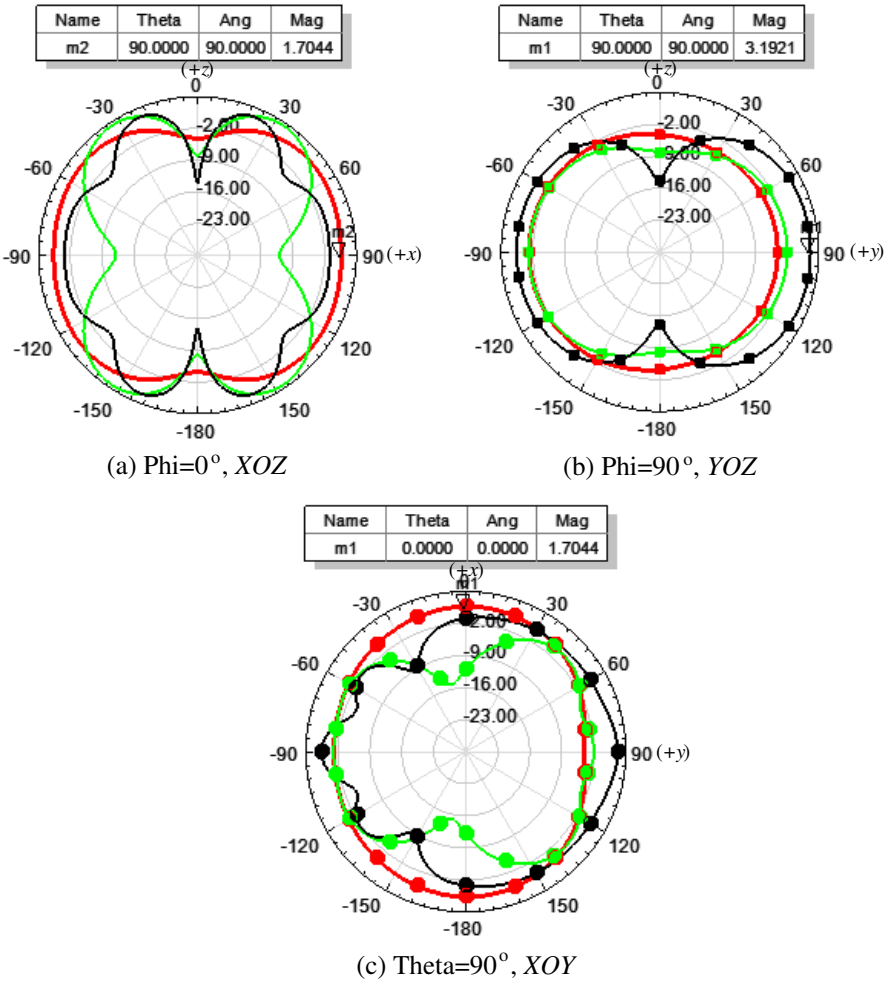

(a) Phi=0°, *XOZ* (b) Phi=90°, *YOZ*

(c) Theta=90°, *XOY*

Figure 10. Gain patterns of K_i at f_3 (bare solid-Phi = 0°, XOZ, E-plane; box marked solid-Phi = 90°, YOZ, H-plane; circle marked solid-Theta = 90°, XOY; $\mathbf{K}_0$-black, $\mathbf{K}_2$-green, $\mathbf{K}_3$-red, as shown in Table 1).

band or wideband, planar or no-planar, and other fractal dipoles only have the normal mode. This phenomenon indicates that circularly curved fractal antenna has very distinct peculiarity.

As presented in Table 1, frequency, input impedance, and percentage bandwidth of each resonance decreases with iteration K_i. The rules and relationships will be formulated next. For convenience, f_{ij} denotes the jth resonant frequency of K_i.

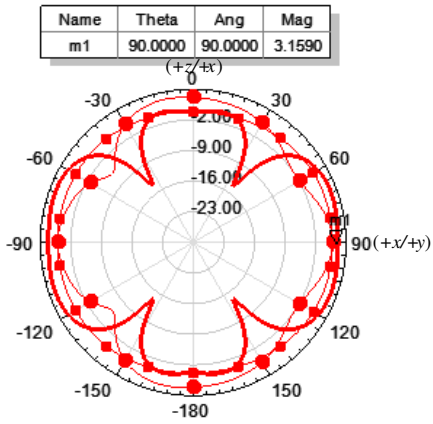

Figure 11. Gain patterns of K_i at f_4 (bare solid-Phi = 0°, XOZ, E-plane; box marked solid-Phi = 90°, YOZ, H-plane; circle marked solid-Theta = 90°, XOY; $\mathbf{K}_3$-red, as shown in Table 1).

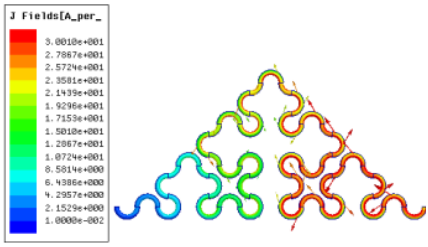

Figure 12. $f_1 = 1.1218\,\text{GHz}$ $(1 \cdot \lambda/2)$.

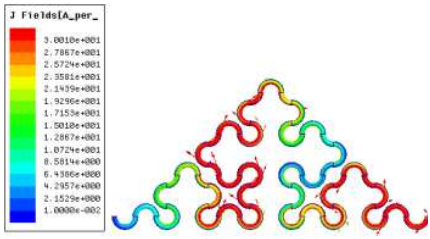

Figure 13. $f_2 = 2.2712\,\text{GHz}$ $(3 \cdot \lambda/2)$.

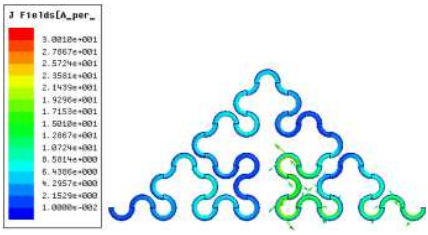

Figure 14. $f_3 = 5.0425\,\text{GHz}$ $(7 \cdot \lambda/2)$.

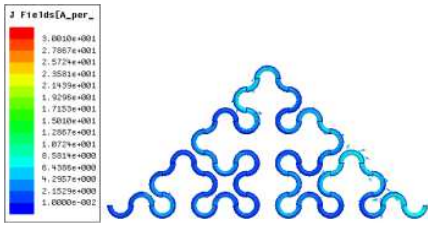

Figure 15. $f_4 = 9.594\,\text{GHz}$ $(15 \cdot \lambda/2)$.

According to the relationship of length and wavelength of straight wire dipole, we can obtain the following formula:

$$\frac{\lambda_{i1}}{2} = \frac{\frac{c}{f_{i1}}}{2} = \left(\prod_{n=0}^{i}\zeta_n\right)^{k\cdot\log[\sigma_i\cdot(|D_{Fi}|+i)]} \cdot (L_0+\varsigma_i) \Rightarrow$$

$$f_{i1} = \frac{c}{2\cdot\left(\prod_{n=0}^{i}\zeta_n\right)^{k\cdot\log[\sigma_i\cdot(|D_{Fi}|+i)]}\cdot(L_0+\varsigma_i)}; \quad (i=0,1,2,\ldots), \quad (9)$$

where c is light speed in free space; ζ_i, D_{Fn}, σ_n are physical scale ratio, fractal dimension and fractal scale ratio of K_i iteration respectively, which can be calculated from formula (5)–(7) as: $\zeta_1 = 1$, $\zeta_2 \approx 1.571$, $\zeta_3 \approx 1.824$; $D_{F1} \approx 0.551$, $D_{F2} \approx 1.284$, $D_{F3} \approx 2.708$; $\sigma_1 = 2.5$, $\sigma_2 \approx 2.333$, $\sigma_3 = 2.2$; $L_0 = 31\cdot\pi$ mm is length of $\mathbf{K}_0$ dipole; ς_n is extra arm length of K_i iteration, $\varsigma_0 = -8$, $\varsigma_1 = -2.4$, $\varsigma_2 = \varsigma_3 = 0.3$ (negative due to parallel segments behave like transmission line); $k = 0.27$ is constant coefficient. The calculated resonances from formula (9) are tabulated in Table 2 with the simulated results for error comparison.

Table 2. Simulated and calculated fundamental resonance of K_i **CAKC** dipole ($\varsigma_0 = -8$, $\varsigma_1 = -2.4$, $\varsigma_2 = \varsigma_3 = 0.3$).

K_i	$\mathbf{K}_0$	$\mathbf{K}_1$	$\mathbf{K}_2$	$\mathbf{K}_3$
Sim (GHz)	1.6771	1.5782	1.3774	1.1218
Cal (GHz)	1.6769	1.5780	1.3772	1.1226
Error (%)	0.013%	0.011%	0.003%	0.075%

(**Sim**-simulated, **Cal**-calculated)

As shown in Table 2, the relative errors between the two results are no more than 0.08%, which means better rationality and accuracy of formula (9) than its counterpart in [25]. Resistance and percentage bandwidth of fundamental resonance of each iteration K_i present so complex relationships with geometrical parameters of the fractal curve that we cannot formulate precise expressions.

So far, we can draw some conclusions from the aforementioned analysis as follows:

(1) K_i CAKC dipole shows the same relationship of resonant numbers f_n and iteration times K_i as the Koch/Koch-like [14] counterpart:

$$N = n_{\max} = i+1 \quad (i=0,1,2,\ldots) \quad (10)$$

(2) Ratio of adjacent resonant frequencies δ_n is very approximate to fractal scale ratio σ_n when iterative number is sufficiently

large [14, 26]:

$$\lim_{n\to i+1} \delta_n = \lim_{n\to i+1} \frac{f_{n+1}}{f_n} \approx \sigma_n = 2, \quad n = (1, 2, \ldots, i+1) \tag{11}$$

(3) Resonant resistance R_{in} and impedance bandwidth decreases with iteration. However, for certain iterative case K_i, percentage bandwidth of resonant frequency f_n does not monotonously diminish with n.

(4) Gain of fundamental frequency f_1 consistently degrades slowly with iteration.

(5) K_i ($i \geq 2$) CAKC dipole peculiarly and unprecedentedly manifests normal mode ($0.5 \cdot \lambda$) and axial ($1.5 \cdot \lambda$) mode simultaneously while all conceived dipoles/monopoles have only normal mode with pattern nulls in the axis.

(6) Multiband of K_i ($i \geq 2$) CAKC dipole operates in $k_n \cdot (\lambda/2)$ ($n - f_n,\ k_{n+1} = 2 \cdot k_n + 1,\ k_1 = 1,\ n = 1, 2, \ldots, i+1$) wavelength separately.

(7) Size reduction associates with geometrical scale ζ_i and iteration K_i. Compared with Euclidean counterpart with identical length $L = 4 \cdot (d_0 + r_i)$ and diameter $2 \cdot r_i$, $\mathbf{K}_3$ CAKC and Koch/Koch-like dipole presents 50.27%, 19.31%, and 19.31% size shrinkage at f_1 respectively.

(8) $\mathbf{K}_2$ has most uniform multi-resonant impedances: $R_{in} = 31.8513\,\Omega$ at $f_1 = 1.3774\,\text{GHz}$ (normal mode) and $R_{in} = 37.1771\,\Omega$ at $f_2 = 3.6525\,\text{GHz}$ (axial mode), which means that half-wavelength and half-and-one-wavelength are available simultaneously.

4. $\mathbf{K_2}$ CAKC MONOPOLE ANTENNA

4.1. Physical Design of the Monopole Antenna

CAKC dipole particularly presents normal mode and axial mode simultaneously when $K_i \geq 2$. In addition, in view of geometric complexity and sufficient input impedance, $\mathbf{K}_2$ CAKC folded monopole is chosen as the physical antenna solution. Two $\mathbf{K}_2$ CAKC wires with arc radii $d_2 = 2.5\,\text{mm}$ and section radius $r_0 = 0.75\,\text{mm}$ are connected end-to-end by two circularly arched segments of radius $r_0 = 0.75\,\text{mm}$ for smooth transition. Then, they are coalesced with a horizontal wire of radius $r_0 = 0.75\,\text{mm}$ and length $l = 5\,\text{mm}$, forming a folded CAKC wire. The folded fractal wire is upstanding with height $H = L + h_2 = 39.5\,\text{mm}$ ($0.1725 \cdot \lambda_1$, λ_1-wavelength of $f_1 = 1.31\,\text{GHz}$ in free space). Its two open ends are oriented downwards and jointed

with a copper circular disc of diameter $D_g = 80\,\text{mm}$ $(0.3494 \cdot \lambda_1)$, thickness $T_g = 1\,\text{mm}$, and the inner conductor of a $50\,\Omega$ coaxial cable respectively. The two ends are arranged in the radial direction of the copper disc and evenly separated from its centre, as shown in Fig. 16(b). Folded-arm quadruples the impedance of a dipole and half-arm halves the impedance [27]. Therefore, the folded monopole will have a resonant impedance $Z_{fm} = 2 \cdot Z_d$ (impedance of the CAKC dipole). The monopole can be directly fed with a $50\,\Omega$ coaxial cable without a complicated impedance transformer. For comparison, the $\mathbf{K}_0$ linear counterpart is also studied, as shown in Fig. 16(a).

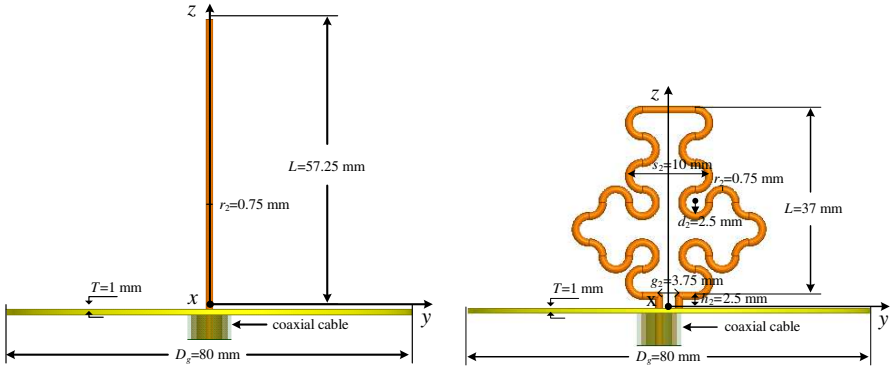

(a) $\mathbf{K}_0$ linear monopole (b) $\mathbf{K}_2$ CAKC folded monopole

Figure 16. Geometry of the two monopoles (unit: mm).

Another reason for the monopole configuration is axial directivity enhancement with a beneath reflection ground plate. What most noteworthy is that this folded configuration is not a loop antenna though it resembles a ring, as the Koch loop [28], so much. The most noticeable discrepancy between them is that the former aims at impedance double and larger bandwidth while the latter targets the large encircled area for axial radiation. The circularly arced fractal wire is fabricated manually with an identical-shaped auxiliary slot cut in a wood board. Next, it is assembled with the circular copper disc, SMA connector, and then fastened with four screw nuts, as shown in Fig. 17.

4.2. Simulation Results and Analysis

Full-wave EM analysis is performed for both $\mathbf{K}_0$ linear monopole and $\mathbf{K}_2$ CAKC folded monopole in 1 GHz–10 GHz. Then, the prototype of

Figure 17. Prototype of $\mathbf{K}_2$ CAKC folded monopole (SMA with 4-holed square flange).

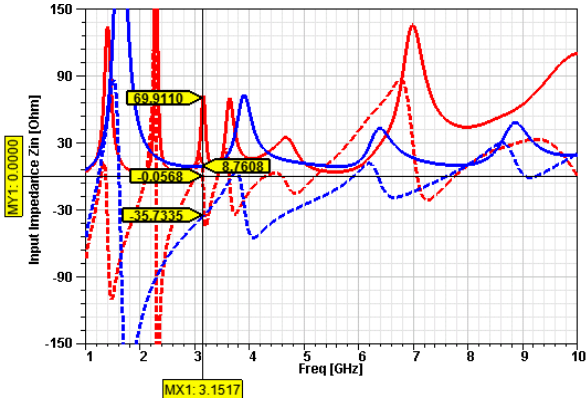

Figure 18. Simulated input impedance Z_{in} of the two monopoles (red-$\mathbf{K}_2$ CAKC folded monopole, blue-$\mathbf{K}_0$ linear monopole; solid-R_{in}, dash-X_{in}).

$\mathbf{K}_2$ CAKC is measured reflection coefficient $|S_{11}|$ with Agilent PNA E8361C vector network analyzer. The measured $|S_{11}|$ and simulated $|S_{11}|$ are merged into Fig. 19 for comparison (solid-measured, dash-simulated).

Figure 18 shows remarkable multi-resonance property in input impedance Z_{in} for the two monopoles. Low and high resonant impedances emerge alternately. The low impedances (34.7 Ω–69.8 Ω) are very approximate to 50 Ω, which means good direct matching with standard coaxial cable for multiband. Accordingly, $|S_{11}|$ of $\mathbf{K}_2$ CAKC presents penta-bands ($|S_{11}| \leq -10$ dB), of which $f_1 = 1.31$ GHz (L-band), $f_2 = 3.14$ GHz (C-band), $f_3 = 3.63$ GHz (WiMAX+C-band), $f_4 = 4.65$ GHz (C-band), and $f_5 = 7.71$ GHz (C-band). In comparison, $|S_{11}|$ of $\mathbf{K}_0$ linear presents quad-bands ($|S_{11}| \leq -8$ dB), of which

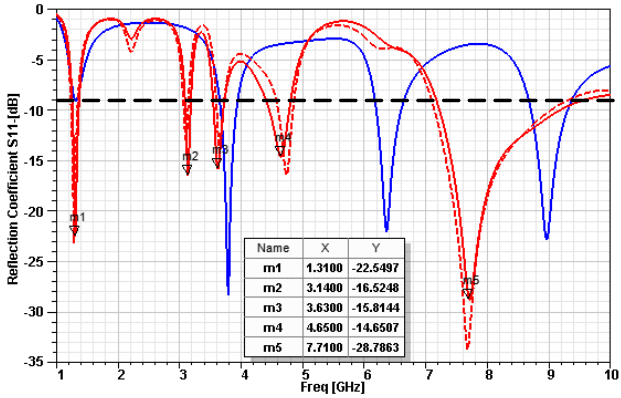

Figure 19. Reflection coefficient $|S_{11}|$ of the two monopoles (solid-simulated; dash-measured; red-$\mathbf{K}_2$ CAKC folded monopole; blue-$\mathbf{K}_0$ linear monopole).

$f_1 = 1.32\,\text{GHz}$, $f_2 = 3.8\,\text{GHz}$, $f_3 = 6.36\,\text{GHz}$, and $f_4 = 8.96\,\text{GHz}$. Besides f_1, the other bands all have higher resonant frequencies than $\mathbf{K}_2$ CAKC, as shown in Fig. 19 and Table 2. Comparably, the simulated (solid line) and measured (dashed line) results of $|S_{11}|$ of $\mathbf{K}_2$ CAKC are quite accordant with each other though the latter shows lower values and slight upper shifting. This is due to fabrication tolerance and inherent error of the measurement systems.

We tabulate the multiband features of the two monopoles in Table 3.

As shown in Table 3, unlike the CAKC dipole counterparts, the adjacent frequency ratios δ_n of $\mathbf{K}_2$ CAKC folded monopole are not equal to the fractal scale ratio σ_n but vary from 2.4 to 1.2, because the five bands are not all produced by the fractal iteration. f_1 is fundamental resonance correlating with the overall dimension, which can be calculated with formula (9). It presents 31% height reduction compared with the $\mathbf{K}_0$ linear wire monopole at f_1 at the cost of lateral extent of 30 mm, as shown in Figs. 16(a)–(b). f_2 and f_4 are resonances yielded by the folded configuration, and f_3 and f_5 are resonances induced by the fractal iteration. If excepting f_2 and f_4, we will get $\delta_{31} = f_3/f_1 = 2.77$, $\delta_{53} = f_5/f_3 = 2.12$, which are consistent with the dipole cases (Table 1) and comply with the theory of fractal antennas [14, 21]. Just like $\mathbf{K}_0$ linear monopole and rectilinear fractal wire antennas, circularly curved fractal wire antennas are also narrow-banded. f_1–f_4 of $\mathbf{K}_2$ CAKC folded monopole are all narrow bands, but f_5 infrequently presents 25.94% ultra-wideband. This indicates that the fractal monopole behaves like a travelling-wave antenna in high resonance.

Table 3. Resonant properties of the two monopoles.

	f_1	f_2	f_3	f_4	f_5
f_i (GHz)	1.31, **1.32**	3.14, **3.8**	3.63, **6.36**	4.65, **8.96**	7.71,
$\delta_{n=f_{n+1}/f_n}$	—	2.397, **2.879**	1.156, **1.674**	1.281, **1.409**	1.658,
R_{in} (Ω)	36.27, **30.08**	69.87, **53.11**	69.51, **42.76**	34.69, **44.96**	46.96,
S_{11} (dB)	−22.55, **−9.17**	−16.52, **−28.35**	−15.81, **−22.08**	−14.65, **−22.88**	−28.79,
BW (−10 dB, MHz)	110, 8.40%; —	100, 3.18%; **256,** **6.74%**	150, 4.13%; **402,** **6.32%**	340, 7.31%; **600,** **6.70%**	2000, 25.94%;
Gain (dBi)	1.83, **1.57**	3.16, **3.70**	10.04, **6.36**	9.81, **7.43**	4.78,

(normal-$\mathbf{K}_2$ CAKC folded monopole, bold-$\mathbf{K}_0$ linear monopole)

We measured radiation patterns of f_1, f_2, f_3, f_4, and f_5 of $\mathbf{K}_2$ CAKC in a 3D anechoic chamber. The simulated and measured patterns are merged into corresponding 2D charts for discrepancy comparison and redundancy avoidance, as illustrated in Fig. 20–Fig. 24. In these patterns, red, green represent H-plane and E-plane, respectively, and bare line and marked line represent Co-polarization (C-Pol) and Cross-polarization (X-Pol), respectively, and solid and dashed lines denote simulated and measured results in sequence. For intuitive understanding of the radiation characteristics, the 3D patterns of the two monopoles are also presented.

As Figs. 20(c)–24(b) show, the measured 2D gain patterns agree with simulated results well. Just like $\mathbf{K}_0$ linear at $f_1 = 1.32$ GHz, $\mathbf{K}_2$ CAKC folded monopole also has ideal dipole-like radiation patterns at $f_1 = 1.31$ GHz, which are omnidirectional in H-plane (Theta = 90°-XOY), doughnut-shaped in E-plane (Phi = 90°-YOZ; V-polarization) with null in axial direction ($+Z$-axis), with peak in the horizon (X/Y-axis), and slightly lower gain $G = 1.83$ dBi, as shown in Fig. 20. Gain patterns at $f_2 = 3.14$ GHz and $f_2 = 3.8$ GHz are also dipole-like (omnidirectional in H-plane, Theta = 90°-XOY; doughnut-shaped in E-plane, Phi = 90°-YOZ; V-polarization). However, the maximum radiations are about 30° elevation tilting from the horizon with moderate gain $G = 3.16$ dBi, as shown in Fig. 21. Gain pattern

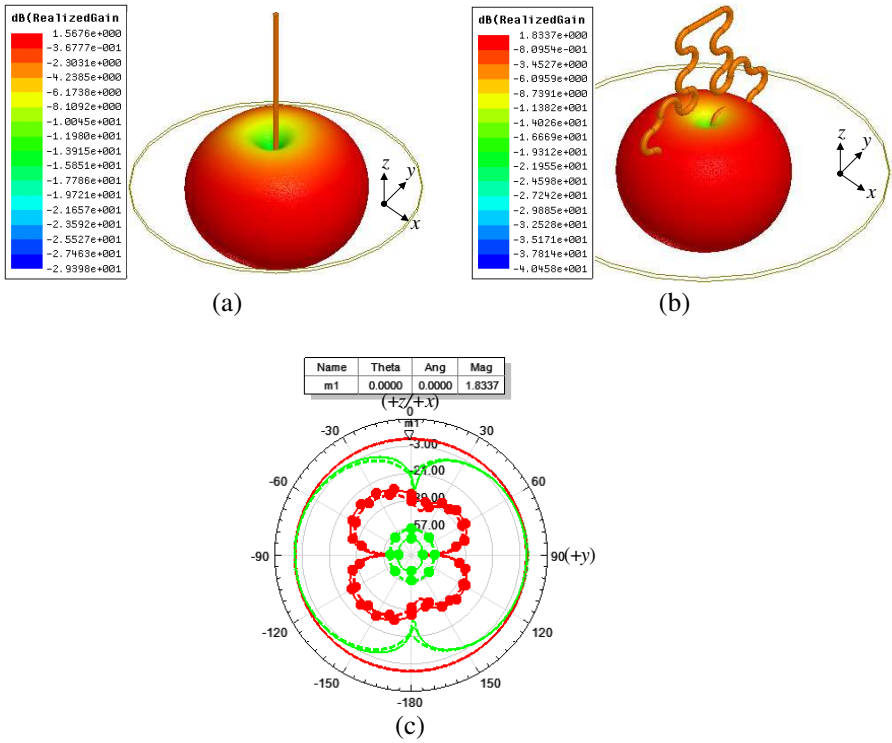

Figure 20. Gain patterns of the two monopoles at f_1. (a) 3D gain pattern of $\mathbf{K}_0$ linear at $f_1 = 1.32\,\text{GHz}$. (b) 3D gain pattern of $\mathbf{K}_2$ CAKC at $f_1 = 1.31\,\text{GHz}$. (c) 2D gain patterns of $\mathbf{K}_2$ CAKC at $f_1 = 1.31\,\text{GHz}$ (normal mode; $G = 1.83\,\text{dBi}$; red-Theta = 90°-XOY, H-plane; green-Phi = 90°-YOZ, E-plane; bare line-C-Pol, marked line-X-Pol; solid-simulated, dash-measured).

at $f_3 = 3.63\,\text{GHz}$ of $\mathbf{K}_2$ CAKC is endfired (H-plane, Phi = 0°-XOZ; E-plane, Phi = 90°-YOZ; V-polarization) with peak radiation in $+Z$-axis, in which the pattern null of the $\mathbf{K}_0$ linear monopole at $f_3 = 6.36\,\text{GHz}$ just occurs, and the gain is as high as $G = 10.03\,\text{dBi}$ (FTBR = 16.8 dBi), as shown in Fig. 22. Gain pattern of $\mathbf{K}_2$ CAKC at $f_4 = 4.65\,\text{GHz}$ is also endfired (H-plane, Phi = 0°-XOZ; E-plane, Phi = 90°-YOZ; V-polarization) with peak radiation in $+Z$-axis and high gain $G = 9.81\,\text{dBi}$ (FTBR = 14.8 dBi). In contrast, the $\mathbf{K}_0$ linear monopole at $f_4 = 8.96\,\text{GHz}$ also presents dipole-like pattern but with larger side lobes, as shown in Fig. 23. The folded monopole behaves just as an axial-mode helix antenna at f_3 and f_4. The major differences between them are polarization and bandwidth. The former is vertical polarization and narrow bandwidth, while the

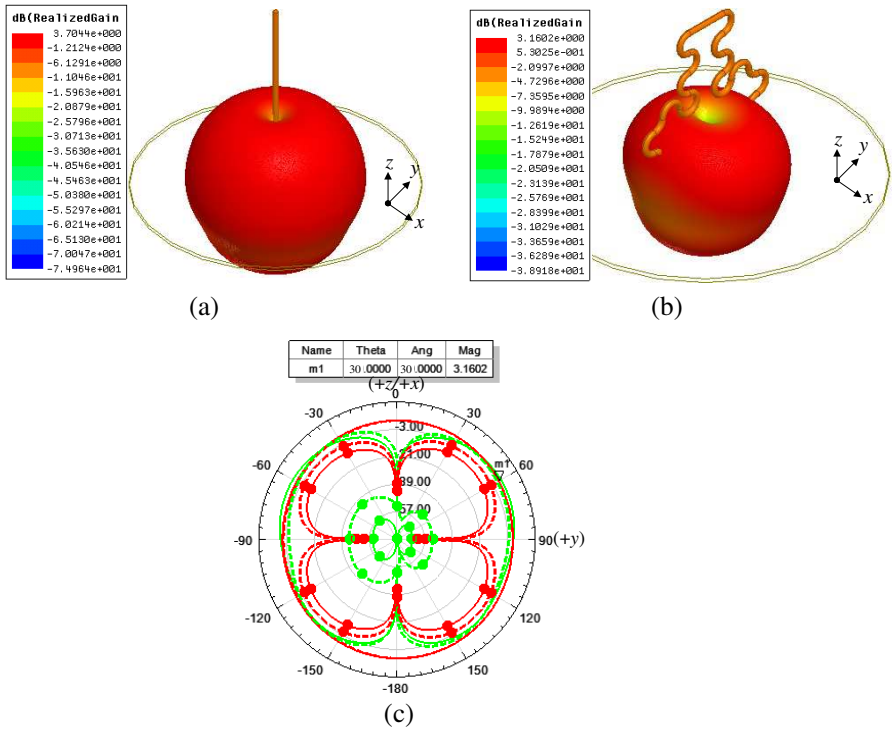

Figure 21. Gain patterns of the two monopoles at f_2. (a) 3D gain pattern of $\mathbf{K}_0$ linear at $f_2 = 3.8$ GHz. (b) 3D gain pattern of $\mathbf{K}_2$ CAKC at $f_2 = 3.14$ GHz. (c) 2D gain patterns of $\mathbf{K}_2$ CAKC at $f_2 = 3.14$ GHz (normal mode; $G = 3.16$ dBi; red-Theta = 30°-XOY, H-plane; green-Phi = 90°-YOZ, E-plane; bare line-C-Pol, marked line-X-Pol; solid-simulated, dash-measured).

latter is circular polarization and broad bandwidth. Gain pattern at $f_5 = 7.71$ GHz is off-endfire (H-plane, Phi = 0°-XOZ; E-plane, Phi = 90°-YOZ; V-polarization) with null not in axial direction, with peak radiation 38° elevation tilting from the horizon, and considerable gain $G = 4.78$ dBi, as shown in Fig. 24.

The normal omni-directivity and axial-directivity have never been possessed simultaneously by any dipoles and monopoles. Helix antenna also has normal mode and axial mode. However, the frequency span between them is quite large. Furthermore, impedances of the two modes are so far different that their matching with a common feedline is very hard. So, the dual-mode operation is unavailable for helix antenna. And this peculiarity is just the most highlight of the fractal folded monopole. Due to geometrical consistency and performance

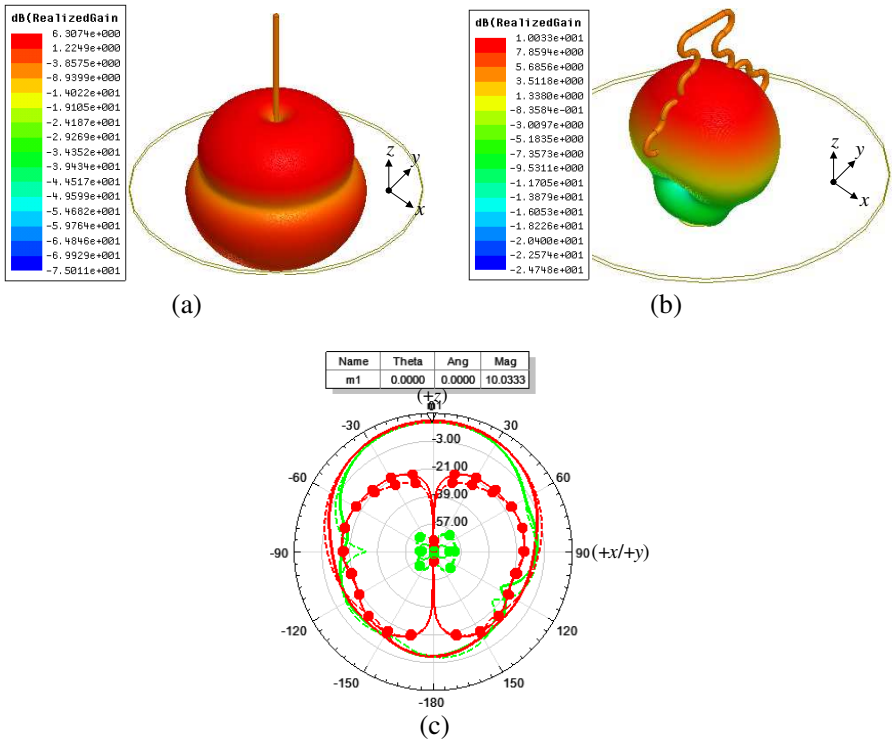

Figure 22. Gain patterns of the two monopoles at f_3. (a) 3D gain pattern of $\mathbf{K}_0$ linear at $f_3 = 6.36\,\text{GHz}$. (b) 3D gain pattern of $\mathbf{K}_2$ CAKC at $f_3 = 3.63\,\text{GHz}$. (c) 2D gain patterns of $\mathbf{K}_2$ CAKC at $f_3 = 3.63\,\text{GHz}$ (axial mode; $G = 10.03\,\text{dBi}$; red-Phi = 0°-XOZ, H-plane; green-Phi = 90°-YOZ, E-plane; bare line-C-Pol, marked line-X-Pol; solid-simulated, dash-measured).

correlativity, $\mathbf{K}_2$ CAKC folded monopole's radiation properties can be observed form its $\mathbf{K}_2$ CAKC dipole counterparts in Section 3. For instance, normal mode of $0.25 \cdot \lambda$ monopole is corresponding to $0.5 \cdot \lambda$ dipole; axial mode of $0.75 \cdot \lambda$ monopole is corresponding to $1.5 \cdot \lambda$ dipole. The discrepancy between Co-polarization and Cross-polarization in E-plane is large, which means good polarization purity. Besides $f_5 = 7.71\,\text{GHz}$, all the patterns shown above possess good azimuthal symmetry owing to quasi circular symmetry of the antenna configuration.

In conclusion, $\mathbf{K}_2$ CAKC folded monopole unprecedentedly manifests three radiation modes simultaneously: axial null, axial peak, and off-axial peak without null, as shown in Figs. 20, 22 and 24 respectively. In comparison, Euclidean or rectilinear fractal dipole or

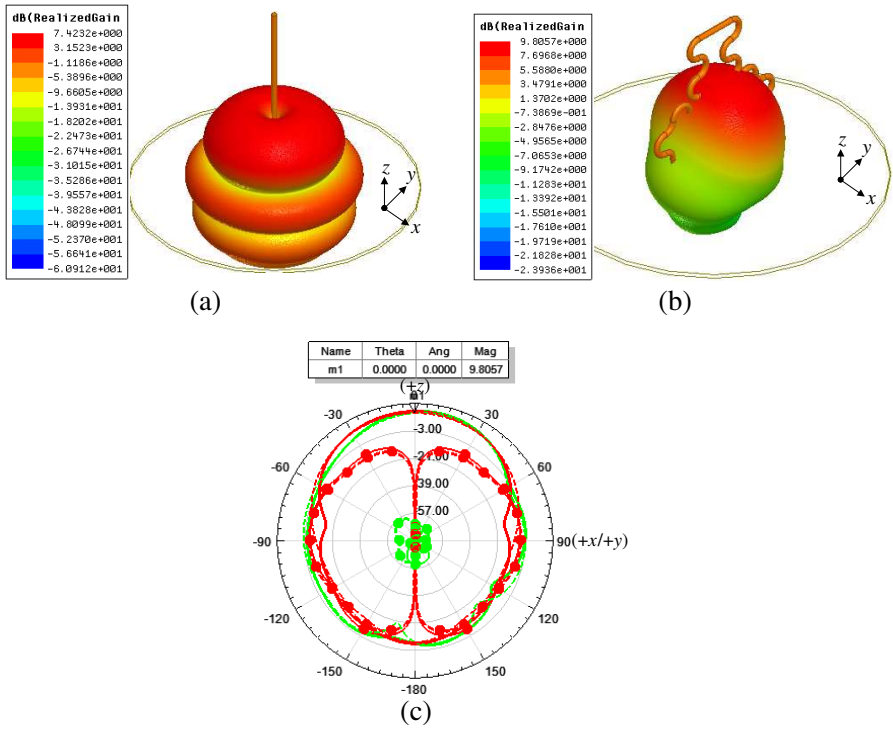

Figure 23. Gain patterns of the two monopoles at f_4. (a) 3D gain pattern of $\mathbf{K}_0$ linear at $f_4 = 8.96\,\text{GHz}$. (b) 3D gain pattern of $\mathbf{K}_2$ CAKC at $f_4 = 4.65\,\text{GHz}$. (c) 2D gain patterns of $\mathbf{K}_2$ CAKC at $f_4 = 4.65\,\text{GHz}$ (axial mode; $G = 9.81\,\text{dBi}$; red-Phi = 0°-XOZ, H-plane; green-Phi = 90°-YOZ, E-plane; bare line-C-Pol, marked line-X-Pol; solid-simulated, dash-measured).

monopole has only normal mode with null in the axis [29, 30]. Helix antenna also has normal mode and axial mode. However, impedance difference and band span of the two modes are very large. Therefore, helix antenna cannot operate in the dual modes with a matching circuit simultaneously.

In addition, unlike the counterparts mentioned above, $\mathbf{K}_2$ CAKC folded monopole does not has side lobe [14, 26], back lobe, and grating lobe in high frequency, as shown in Figs. 22–24. The reason is that circularly cured wire has more flexible and multiform current distribution than straight and linearly bended wires. The $\mathbf{K}_2$ CAKC folded monopole can also be configured into other forms, such as array for high gain [31–33], crossing of two elements [34] for double linear polarizations or circular polarization.

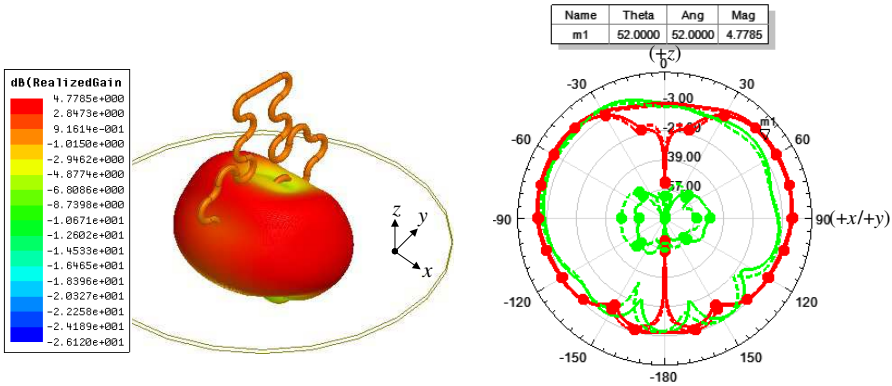

(a) (b)

Figure 24. Gain patterns of $\mathbf{K}_2$ CAKC folded monopole at $f_5 = 7.71$ GHz. (a) 3D gain pattern. (b) 2D gain patterns (off-axial mode; $G = 4.78$ dBi; red-Phi = 0°-XOZ, H-plane; green-Phi = 90°-YOZ, E-plane; bare line-C-Pol, marked line-X-Pol; solid-simulated, dash-measured).

5. CONCLUSION

Circularly arced Koch fractal curve (CAKC) is originally proposed. The new fractus is analyzed mathematically and fractal dimension D_T, physical scale ratio ζ_i and fractal scale ratio σ_i, which dominate the geometrical properties of a fractal, here are found equal. Then, we experimentally investigated CAKC fractal wire dipole of each iteration for fractal features unveiling. Simulation results show that the fractal dipole peculiarly presents multiband and multimode radiation just when iteration number $K_i \geq 2$ ($i \geq 2$). It behaves as an ordinary $0.5 \cdot \lambda$ dipole with doughnut-shaped patterns at the fundamental frequency f_1. But it presents axial radiation on $1.5 \cdot \lambda$ operation at f_3, which had never been possessed by a dipole of various types before. The K_i ($i \geq 2$) CAKC fractal dipole always operates as an odd times of half-wavelength in the multiband. The contiguous frequency ratio δ_n is very approximate to the fractal scale ratio σ_i.

Then, we configured the $\mathbf{K}_2$ CAKC fractal wire into a folded monopole with a circular disc copper ground plate. Thereupon, we obtain omnidirectional coverage in normal direction and directive pointing in axial direction with high gain. Any existent dipole and monopole, no matter broadband [35–37] or narrow band, single band or multiband [38], planar or no-planar, element or array, Euclidean-shaped or fractal-shaped, only has normal omni-directional radiation. This is a great upgrade for dipole antennas. It no longer operates

only on half-wavelength ($0.5 \cdot \lambda$) for omni-directivity but also on half-and-one-wavelength ($1.5 \cdot \lambda$) for high directivity. And that will further diversify applications of this well-known antenna type.

The proposed $\mathbf{K}_2$ CAKC folded monopole has penta-bands ($|S_{11}| \leq -10\,\text{dB}$) with direct coaxial feeding, of which $f_1 = 1.31\,\text{GHz}$ (110 MHz, 8.4%, L-band), $f_2 = 3.14\,\text{GHz}$ (100 MHz, 3.18%, C-band), $f_3 = 3.63\,\text{GHz}$ (150 MHz, 4.13%, WiMAX+C-band), $f_4 = 4.65\,\text{GHz}$ (340 MHz, 7.31%, C-band), and $f_5 = 7.71\,\text{GHz}$ (2000 MHz, 25.94%, C-band). Compared with $\mathbf{K}_0$ linear monopole, this fractal monopole presents 31% height reduction. It has dipole-like radiation patterns at f_1 and f_2 with gain $G = 1.83\,\text{dBi}$, 3.16 dBi respectively; axial radiation patterns at f_3 and f_4 with gain as high as 10 dBi, which has never been realized by any dipoles and monopoles up to now; off-axial radiation patterns at f_5 with gain $G = 4.78\,\text{dBi}$.

Gain patterns of these bands all have broad main lobes and low back lobes without side lobes and grating lobes. In contrast, $\mathbf{K}_0$ linear monopole presents big side lobes in high resonance. In addition, all the bands are vertically polarized with E-plane in YOZ (Phi = 90°). The nice radiation patterns could be attributed to more various current distributions on the circularly arced wire than on straight or linearly bended wires. Moreover, the fractal monopole possesses compactness, lightweight, simpleness, and low cost. So, it is a very attractive candidate for multiband and multi-function antennas, such as satellite antennas, of which normal omni-directional mode and axial directive mode is needed for beaconing and point-to-point communications separately.

ACKNOWLEDGMENT

This work was supported by NSFC (61234001) and the 973 Program of China (2009CB320202).

REFERENCES

1. Cohen, N., "Fractal antennas: Part 1," *Communications Quarterly*, 7–22, Aug. 1995.
2. Cohen, N., "Fractal antenna applications in wireless telecommunications," *IEEE Electronics Industries Forum of New England*, 43–49, May 1997.
3. Werner, D. H., R. L. Haup, and P. L. Werner, "Fractal antenna engineering: The theory and design of fractal antenna arrays," *IEEE Antennas and Propagation Magazine*, Vol. 41, No. 5, 37–58, Oct. 1999.

4. Werner, D. H. and S. Ganguly, "An overview of fractal antenna engineering research," *IEEE Antennas and Propagation Magazine*, Vol. 45, No. 1, 38–57, Feb. 2003.
5. Gianvitorio, J. and Y. Rahmat, "Fractal antennas: A novel antenna miniaturization technique and applications," *IEEE Antennas and Propagation Magazine*, Vol. 44, No. 1, 20–36, Feb. 2002.
6. Anguera, J., C. Puente, C. Borja, and J. Soler, "Fractal-shaped antennas: A review," *Wiley Encyclopedia of RF and Microwave Engineering*, Vol. 2, 1620–1635, Apr. 2005.
7. Liu, Y., S. Gong, and D. Fu, "The advances in development of fractal antennas," *Chinese Journal of Radio Science*, Vol. 17, No. 1, Feb. 2002.
8. Puente, C., J. Romeu, R. Pous, and A. Cardama, "On the behavior of the Sierpinski multiband fractal antenna," *IEEE Transactions on Antennas and Propagation*, Vol. 46, 517–524, Apr. 1998.
9. Sinha, S. N. and M. Jain, "A self-affine fractal multiband antenna," *IEEE Antennas and Wireless Propagation Letters*, Vol. 6, 110–112, Apr. 2007.
10. Manimegalai, B., S. Raju, and V. Abhaikumar, "A multifractal Cantor antenna for multiband wireless applications," *IEEE Antennas and Wireless Propagation Letters*, Vol. 8, 359–362, Aug. 2009.
11. Mandelbrot, B. B., *The Fractal Geometry of Nature*, 2nd Edition, W. H. Freeman, New York, 1983.
12. Falconer, K., *Fractal Geometry: Mathematical Foundations and Applications*, 2nd Edition, John Wiley & Son, Inc, New York, 2003.
13. Baliarda, C. P., J. Romeu, and A. Cardama, "The Koch monopole: A small fractal antenna," *IEEE Transactions on Antennas and Propagation*, Vol. 48, No. 11, 1773–1781, Nov. 2000.
14. Li, D. and J. F. Mao, "A Koch-like sided bow-tie fractal dipole antenna," *IEEE Transactions on Antennas and Propagation*, Vol. 60, No. 5, 40–49, May 2012.
15. Mirzapour, B. and H. R. Hassani, "Size reduction and bandwidth enhancement of snowflake fractal antenna," *IET Microwaves, Antennas and Propagation*, Vol. 2, No. 2, 180–187, Mar. 2008.
16. Mahatthanajatuphat, C., S. Saleekaw, P. Akkaraekthalin, and M. Krairiksh, "A rhombic patch monopole antenna with modified Minkowski fractal geometry for UMTS, WLAN, and mobile

WiMAX application," *Progress In Electromagnetics Research*, Vol. 89, 57–74, 2009.

17. Oraizi, H. and S. Hedayati, "Miniaturized UWB monopole microstrip antenna design by the combination of Giusepe Peano and Sierpinski carpet fractals," *IEEE Antennas and Wireless Propagation Letters*, Vol. 10, 67–70, 2011.
18. Ghatak, R., A. Karmakar, and D. R. Poddar, "A circularshaped Sierpinski carpet fractal UWB monopole antenna with band rejection capability," *Progress In Electromagnetics Research C*, Vol. 24, 221–234, 2011.
19. Ghatak, R., A. Karmakar, and D. R. Poddar, "Hexagonal boundary Sierpinski carpet fractal shaped compact ultrawideband antenna with band rejection functionality," *Int J. Electron Commun (AEÜ)*, Vol. 67, 250–255, 2013.
20. Li, D. and J. F. Mao, "Sierpinskized Koch-like sided multifractal dipole antenna," *Progress In Electromagnetics Research*, Vol. 130, 204–227, Aug. 2012.
21. Vinoy, K. J., "Fractal shaped antenna elements for wide and multiband wireless applications," [D] The Graduate School College of Engineering, The Pennsylvania State University, Aug. 2002.
22. Zhu, J., A. Hoorfar, and N. Engheta, "Peano antennas," *IEEE Antennas and Wireless Propagation Letters*, Vol. 3, 71–74, 2004.
23. Gonzalez-Arbesu, J. M., S. Blanch, and J. Romeu, "The Hilbert curve as a small self-resonant monopole from a practical point of view," *Microwave and Optical Technology Letters*, Vol. 39, No. 1, 45–49, Oct. 2003.
24. Zhu, J., A. Hoorfar, and N. Engheta, "Bandwidth, cross polarization and feed-point characteristics of matched Hilbert antennas," *IEEE Antennas and Wireless Propagation Letters*, Vol. 2, No. 1, 2–5, Jan. 2003.
25. Vinoy, K. J., J. K. Abraham, and V. K. Varadan, "On the relationship between fractal dimension and the performance of multi-resonant dipole antennas using Koch curves," *IEEE Transactions on Antennas and Propagation*, Vol. 51, No. 9, 2296–2303, Sep. 2003.
26. Li, D. and J. F. Mao, "Koch-like sided Sierpinski gasket multifractal dipole antenna," *Progress In Electromagnetics Research*, Vol. 26, 399–427, Apr. 2012.
27. http://www.radio-electronics.com/info/antennas/dipole/folded_dipole.php.

28. Patnam, R. H., "Broadband CPW-fed planar Koch fractal loop antenna," *IEEE Antennas and Wireless Propagation Letters*, Vol. 7, No. 2, 429–431, May 2008.
29. Mustafa, K. T., "Combined fractal dipole wire antenna," *The Second International ITG Conference on Antennas*, Vol. 2, 176–180, Mar. 2007.
30. Best, S. R., "A discussion on the significance of geometry in determining the resonant behavior of fractal and other non-Euclidean wire antennas," *IEEE Antennas and Propagation Magazine*, Vol. 45, No. 3, 9–28, Jun. 2003.
31. Werner, D. H., R. L. Haupt, and P. L. Werner, "Fractal antenna engineering: The theory and design of fractal antenna arrays," *IEEE Antennas and Propagation Magazine*, Vol. 41, No. 5, 37–58, Oct. 1999.
32. Siakavara, K., "Hybrid-fractal direct radiating antenna arrays with small number of elements for satellite communications," *IEEE Transactions on Antennas and Propagation*, Vol. 58, No. 6, 2102–2106, Jun. 2010.
33. Werner, D. H., W. Kuhirun, and P. L. Werner, "The Peano-Gosper fractal array," *IEEE Transactions on Antennas and Propagation*, Vol. 51, No. 8, 2063–2072, Aug. 2003.
34. Altshuler, E. E., "Hemispherical coverage using a double-folded monopole," *IEEE Transactions on Antennas and Propagation*, Vol. 44, No. 8, 1112–1119, Aug. 1996.
35. Jung, J., K. Seol, W. Choi, and J. Choi, "Wideband monopole antenna for various mobile communication applications," *Electronics Letters*, Vol. 41, No. 24, 1313–1214, Nov. 2005.
36. Lee, W. S., K. S. Oh, and J. W. Yu, "A wideband planar monopole antenna array with circular polarized and band-notched characteristics," *Progress In Electromagnetics Research*, Vol. 128, 381–398, 2012.
37. Liu, J., K. P. Esselle, S. G. Hay, and S. S. Zhong, "Study of an extremely wideband monopole antenna with triple band-notched charactersistics," *Progress In Electromagnetics Research*, Vol. 123, 143–158, 2012.
38. Xu, H. X., G. M. Wang, Y. Y. Lv, M. Q. Qi, X. Gao, and S. Ge, "Multifrequency monopole antennas by loading metamaterial transmission lines with dual-shunt branch circuit," *Progress In Electromagnetics Research*, Vol. 137, 705–725, 2013.